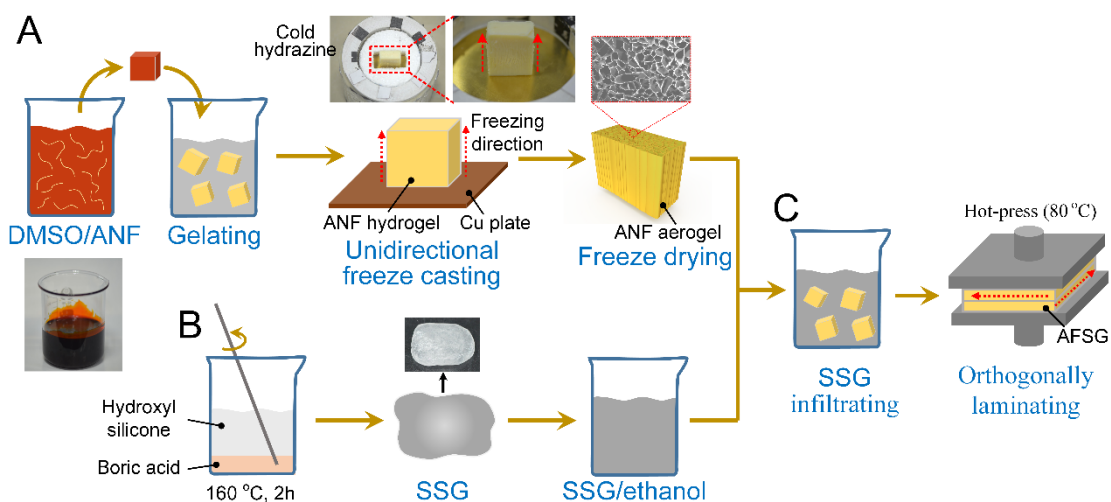**Supplemental information**

A lightweight aramid-based structural composite with ultralow thermal conductivity and high-impact force dissipation

Jianpeng Wu, Yu Wang, Junshuo Zhang, Chunyu Zhao, Ziyang Fan, Quan Shu, Xiaokang He, Shouhu Xuan, and Xinglong Gong

Figure S1. Preparation of AFSG. Detailed preparation process of (A) ANF aerogel, (B) SSG/ethanol dispersion, and (C) AFSG.

The detailed preparation process of AFSG was shown in Figure S1. Firstly, the dark red ANF dispersion was prepared by deprotonation of aramid fabrics in dimethyl sulfoxide (DMSO) solvent and then transferred into deionized water for gelation (Figure S1A left side), in which DMSO was removed thoroughly accompanied with the formation of intermolecular hydrogen bonds among ANF. The ANF hydrogel was further contacted with a cold source (copper plate, -70 $^{\circ}$C) cooled with liquid nitrogen (Figure S1A middle). Driven by the temperature gradient between liquid nitrogen and ANF hydrogel, a large number of ice crystals grew perpendicular to the cold source and occupied internal space of homogenous hydrogel, squeezing the ANF into anisotropic scaffolds (Figure 1A left side). After freeze drying at -50 $^{\circ}$C and 10 Pa for 48 h, ice crystals gradually sublimated from the hierarchical porous networks of ANF aerogel (Figure 2A and Figure S1A right side). In addition, SSG was prepared by mixing hydroxyl silicone and boric acid in 160 $^{\circ}$C for 2h (Figure S1B left side). Then, SSG was mixed with ethanol (mass ratio, 2:1) to obtain homogeneous SSG/ethanol dispersion (Figure S1B right side). The dispersion was infiltrated into the oriented scaffolds of ANF aerogel to thoroughly fill the microscale pores (Figure 1A middle and Figure S1C left side), where the self-supporting ANF scaffolds provided effective restraint for internal filler. After compounding with SSG, two pieces of same ANF aerogel were orthogonally laminated at 80 $^{\circ}$C to densify the porous networks and remove residual ethanol (Figure 1A right side and Figure S1C right side). According to the procedure, all prepared AFSGs possessed pale yellow appearances, void-SSG coexistence microstructures, and similar densities (0.46 ± 0.02 g cm^{-3}).
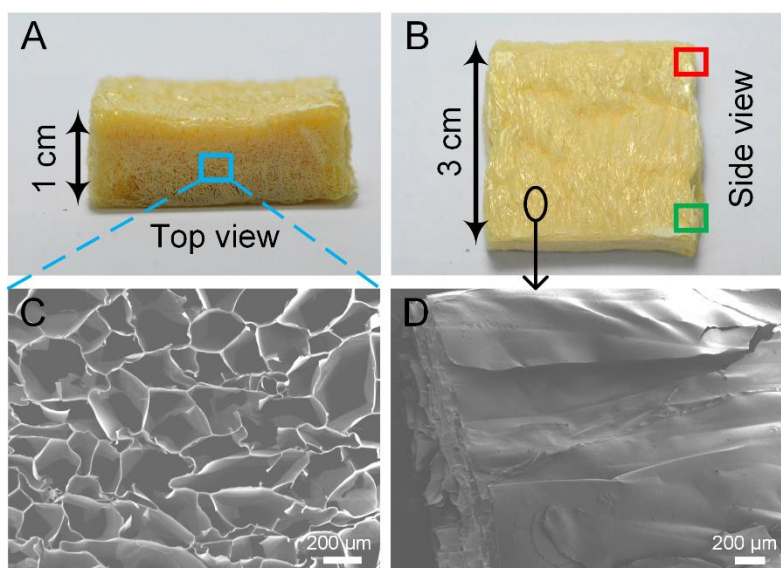
Figure S2. Characterization of ANF aerogel. (A) Top view and (B) side view of ANF aerogel. SEM image of (C) the honeycomb porous scaffold and (D) the exterior ANF sheets.
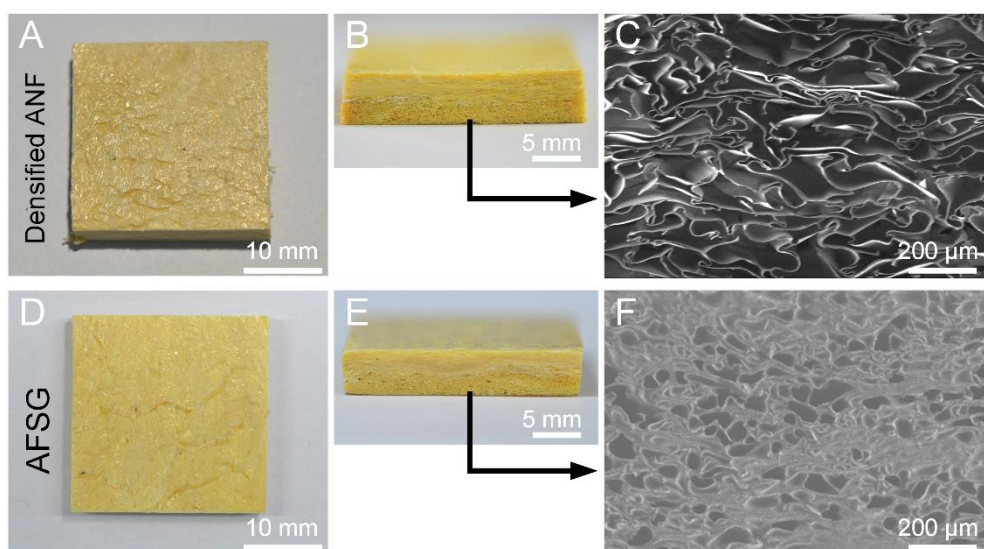

Figure S3. Characterizations of densified ANF block and AFSG. Optical photographs of (A-B) densified ANF block and (D-E) AFSG. SEM images of partial cross-section of (C) densified ANF block and (F) AFSG.
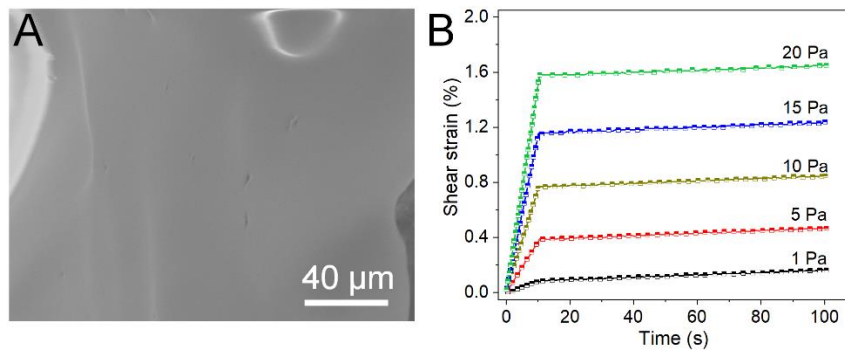
Figure S4. Characterization of SSG. (A) SEM images of SSG. (B) Creep curves of SSG under different shear stresses. All shear stresses were applied instantaneously at 0 s and released after 10 s.
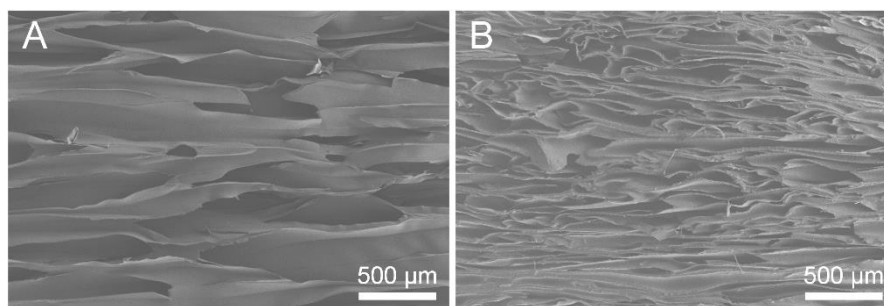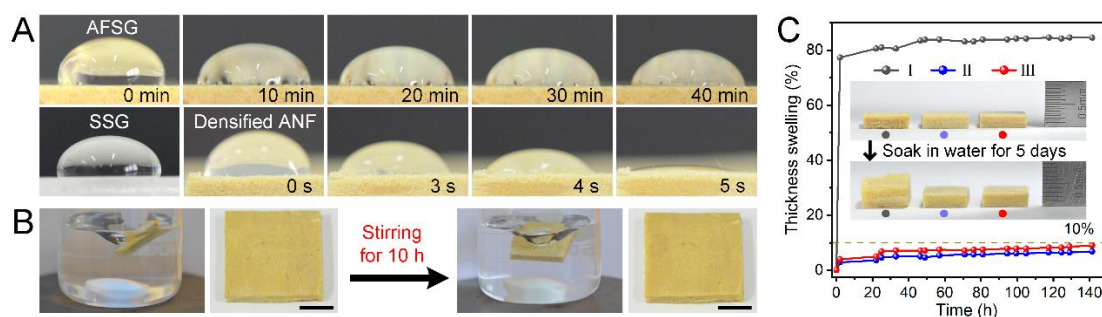

Figure S5. Comparison of microstructure between ANF aerogel and AFSG. Cross-sectional SEM images of (A) ANF aerogel and (B) AFSG in side view.
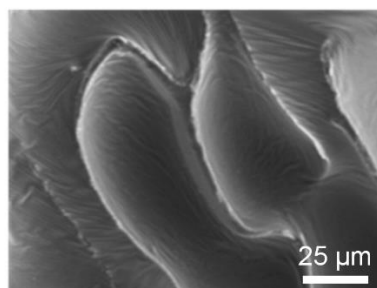
Figure S6. Enlarged view of cross-sectional SEM image of AFSG.
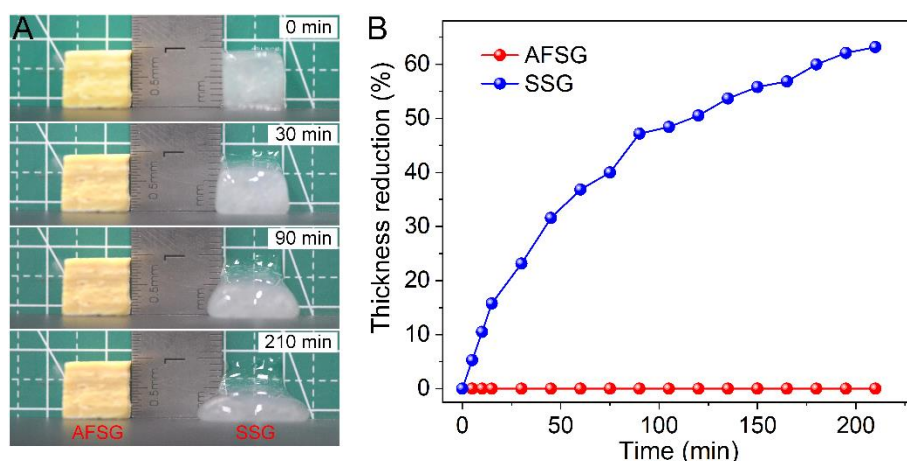
Figure S7. Comparison of creep behavior between AFSG and SSG. (A) Optical images of AFSG and SSG and (B) corresponding thickness reductions over time.

Figure S8. Water resistance performance of AFSG. (A) The hydrophilic performance of AFSG, densified ANF block, and SSG. (B) Morphology change of AFSG after magnetic stirring in water for 10 h with 540 rpm (Scale bars, 10 mm). (C) Thickness swelling of monolayer densified ANF block (sample I), monolayer densified ANF@SSG (sample II), and AFSG (sample III) after soaking in water for 140 h. (Insets illustrated the thickness changes of all samples.)

The hydrophobicity was evaluated by observing water contact angle (Figure S8A). SSG had favorable water-proof property due to the abundant inert groups (Si-O-Si) in hydroxyl silicone oil molecular chains. Whereas the polar N-H groups of ANF chains (Figure 1D) resulted in obvious hydrophilic feature of densified ANF block as a water drop rapidly penetrated into the internal voids within 5 s (Figure S8A). By virtue of the adhesion of SSG on ANF pore walls, AFSG acquired a notable improvement in hydrophobicity, because the water drop kept a high contact angle with its surface even after 40 min (Figure S8A). It also exhibited robust water shock resistance behavior as the morphology change was negligible after stirring violently for 10 h (Figure S8B). Anti-swelling performance was further investigated. Three samples, monolayer densified ANF block, monolayer densified ANF@SSG, and AFSG, were soaked in water simultaneously for 5 days to evaluate their swelling effect. In comparison with the fast expansion of monolayer densified ANF block, both the thickness swelling of monolayer densified ANF@SSG and AFSG increased slowly over time and did not exceed 10% even after 140 h (Figure S8C). The excellent anti-swelling capacity of AFSG indicated strong adhesion between SSG cores and ANF scaffolds as well as tight bonding at laminated interface, which

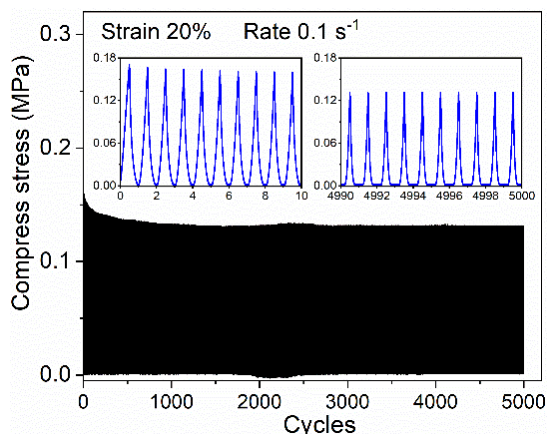was helpful for its applications in humid environment.

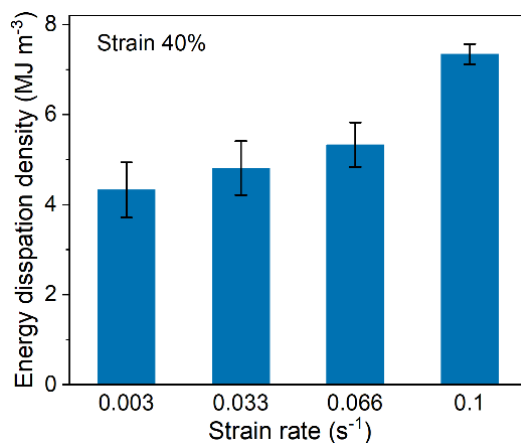**Figure S9. Cyclic compression of densified ANF block under 20% strain at 0.1 s^{-1} strain rate.**

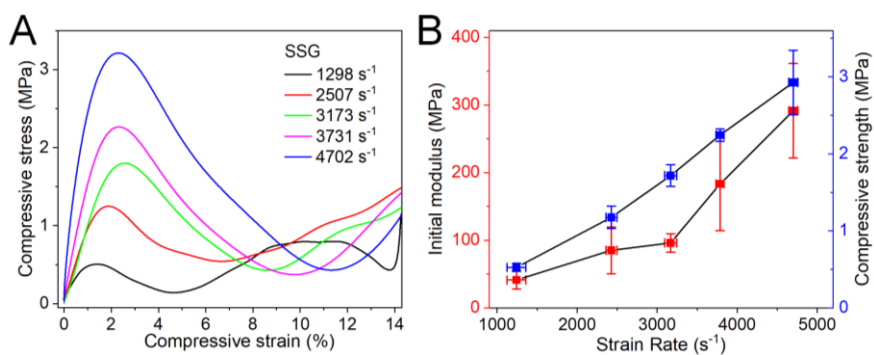**Figure S10. Rate-dependent energy dissipation density of AFSG.**
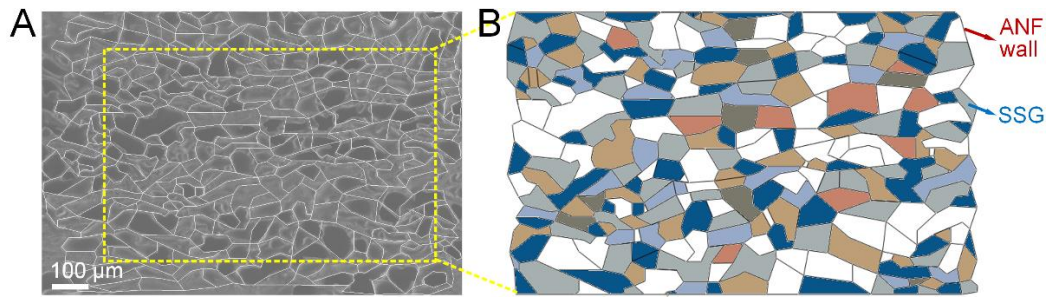

Figure S11. Rate-dependent compressive behavior of SSG. (A) True stress-strain curves of SSG under different strain rate. (B) The dependence of initial modulus and compressive strength on strain rate of SSG.

Figure S12. Construction of void-SSG model of AFSG. (A) Cross-sectional SEM image of AFSG. The white contour lines represented ANF scaffolds. (B) Corresponding reconstructed AFSG microstructure.
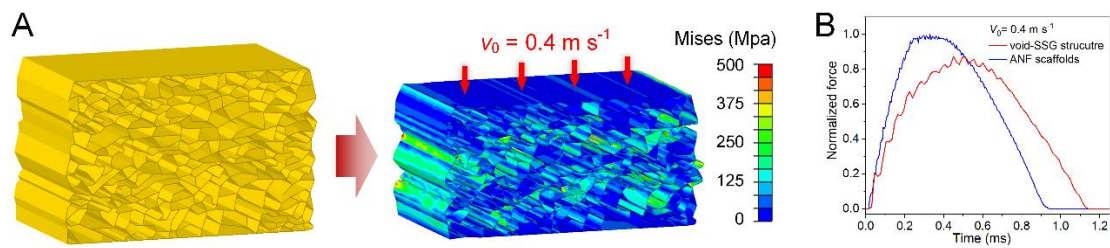
Figure S13. FEM simulation of impact process. (A) FEM of ANF scaffolds extracted from voids-SSG structure and corresponding Mises stress distribution under maximum impact deformation with an initial velocity of 0.4 m s^{-1}. (B) FEM results of normalized contact force between objects (void-SSG FEM and ANF scaffolds FEM) and ground during impact process.
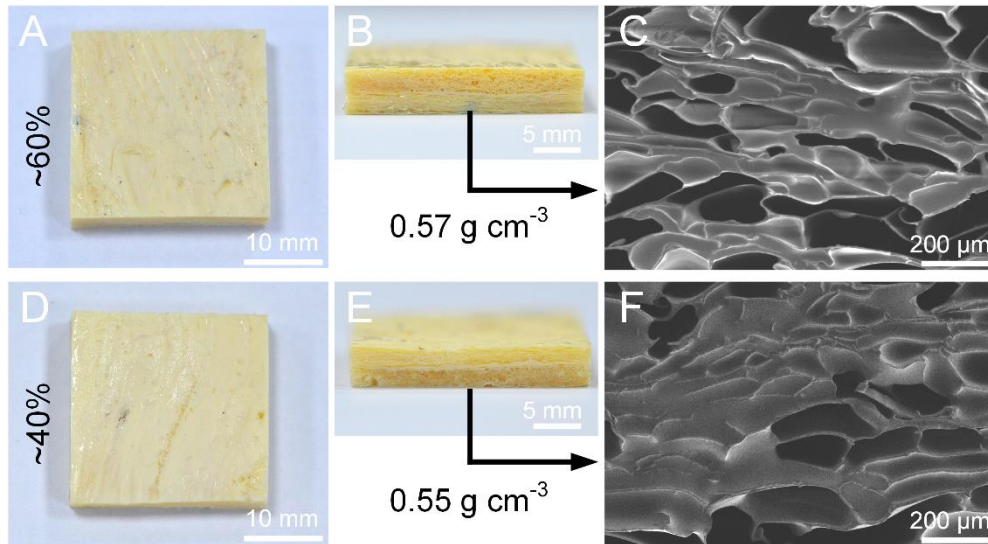
Figure S14. Characterizations of AFSGs with different densification levels. Optical photographs of AFSGs under (A-B) ~60% compression and (D-E) ~40% compression. Cross-sectional SEM images of AFSGs under (C) ~60% compression and (F) ~40% compression.
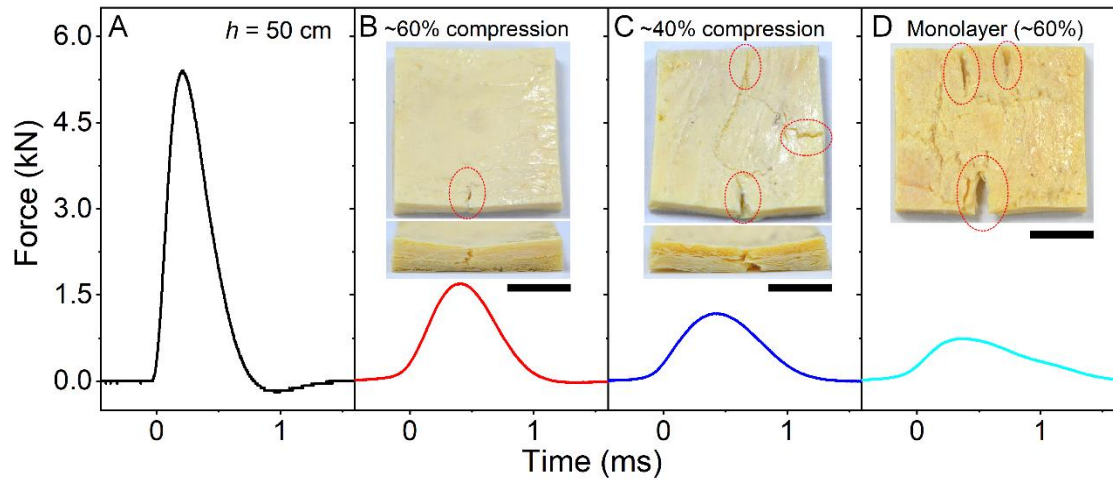
Figure S15. Anti-impact performances of AFSGs with different densification levels and layer structures. Force-time curves of (A) reference condition, (B) AFSG under ~60% compression, (C) AFSG under ~40% compression, and (D) monolayer AFSG under ~60% compression, respectively, during impact process from 50 cm height. (The insets represented surface morphologies of samples after impact. Red circles represented the cracks. Scale bars, 10 mm)
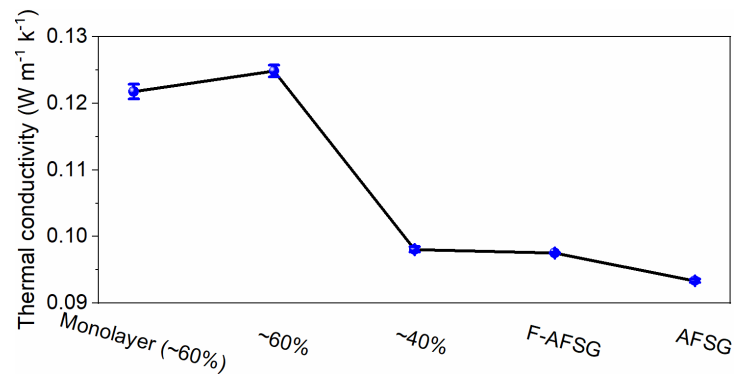
Figure S16. Thermal conductivities of monolayer AFSG under ~60% compression, AFSG under ~60% compression, AFSG under ~40% compression, F-AFSG, and AFSG, respectively.
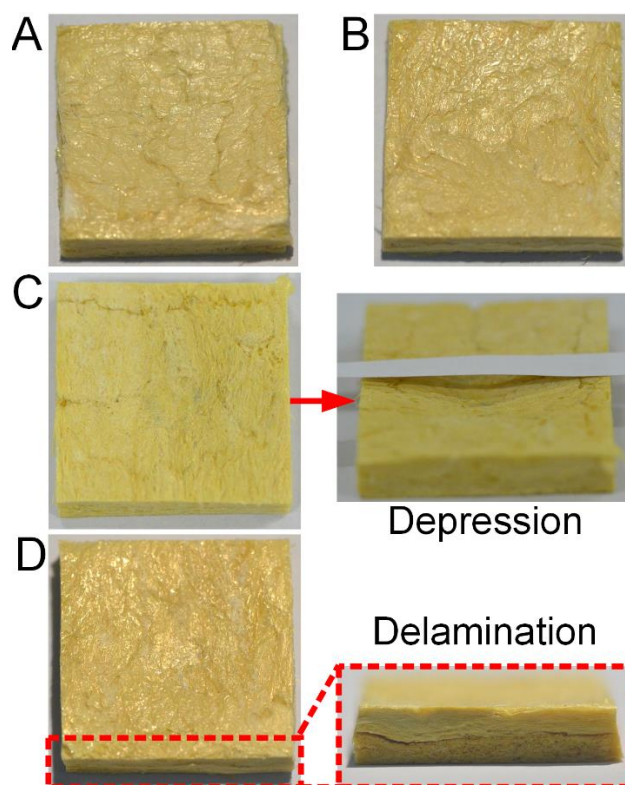
Figure S17. Surface morphologies of densified ANF blocks after impact. The impact heights were (A) 10 cm, (B) 30 cm, (C) 50 cm, and (D) 70 cm, respectively. All specimens had an original dimension of 25×25×5 mm^3.
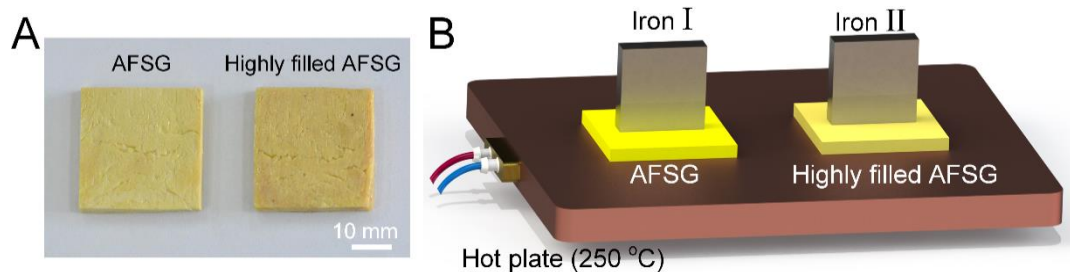
Figure S18. Comparison of thermal insulation property between AFSG and highly filled AFSG. (A) Photographs of AFSG and highly filled AFSG. (B) Schematic illustrating the heating process of iron blocks placed on AFSG and highly filled AFSG, respectively.
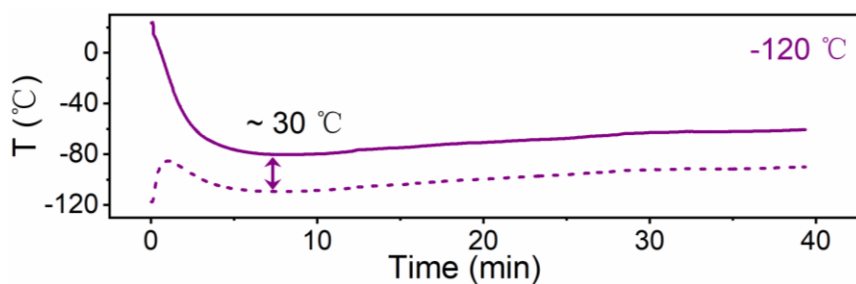
Figure S19. Temperature difference between AFSG surface (solid line) and cold plate (dotted lines). The cold plate was cooled by liquid nitrogen.

Figure S20. Optical images showing the morphologies of AFSG and poplar wood after heating at 300ºC for 30 min. The wood has sever surface carbonization along with bulking while AFSG remained almost intact.
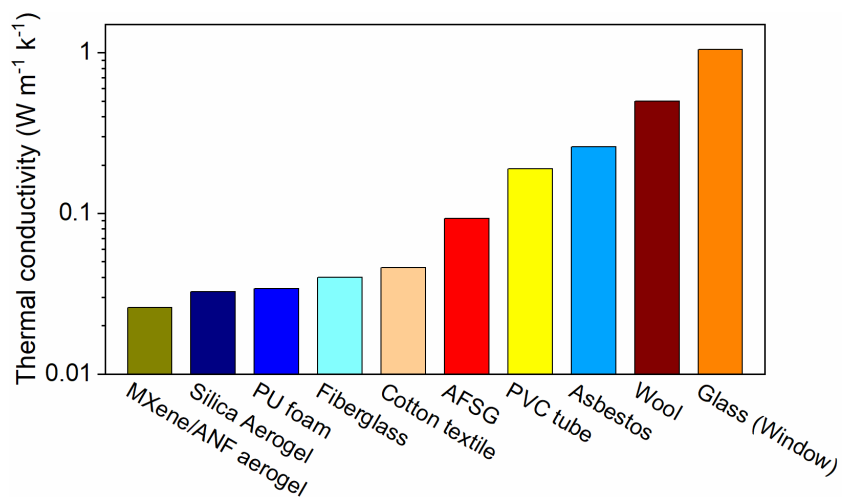
Figure S21. Comparison of thermal conductivity among common thermal insulators, aerogels, and AFSG.[1-8]
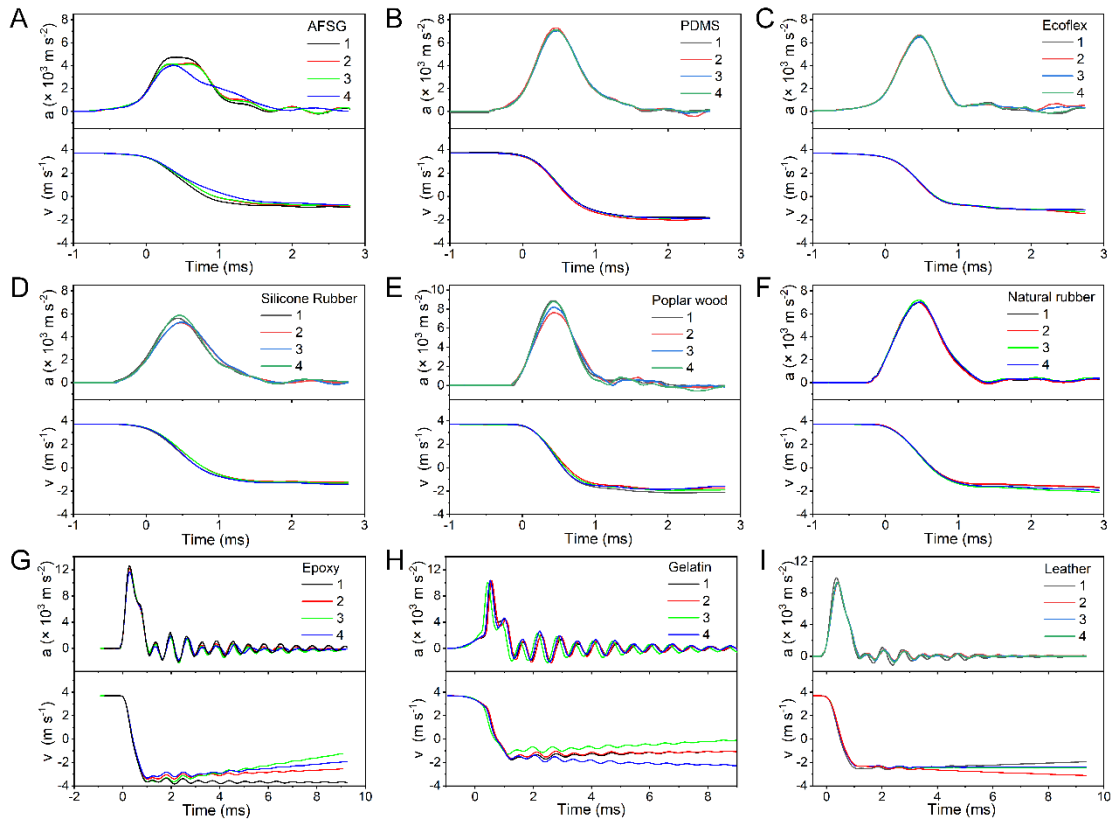
Figure S22. Acceleration signals (*a*) and corresponding integral velocities (*v*) of drop hammer during impact processes. These impact actions were conducted on (A) AFSG, (B) PDMS, (C) Eco-flex, (D) silicone rubber, (E) poplar wood, (F) natural rubber, (G) epoxy, (H) gelatin, and (I) leather, respectively. The drop height was 70 cm. All specimens had a dimension of $25 \times 25 \times 5$ mm^3. The evaluation of energy absorption of all specimens were described in note S2.
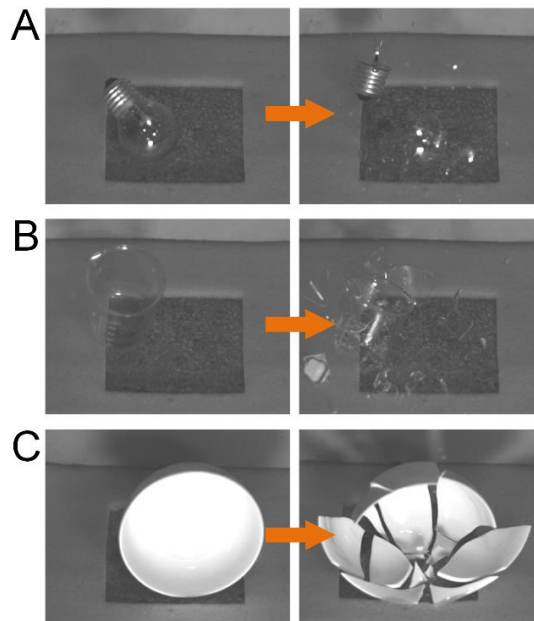
Figure S23. Snapshots of (A) bulb, (B) beaker, and (C) bowl hitting floor that freely dropped from 2 m height.
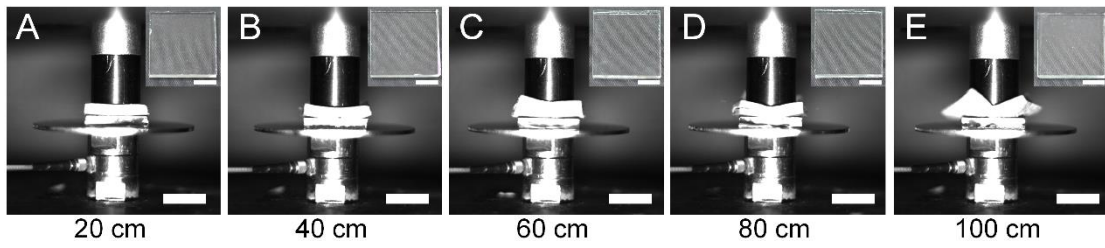
Figure S24. Snapshots of drop hammer impacting glasses. These glasses were protected with AFSG from (A) 20 cm, (B) 40 cm, (C) 60 cm, (D) 80 cm, and (E) 100 cm, respectively (see also Video S4). Scale bars, 20 mm. (Insets showed the unbroken glasses after impact. Scale bars, 10 mm)
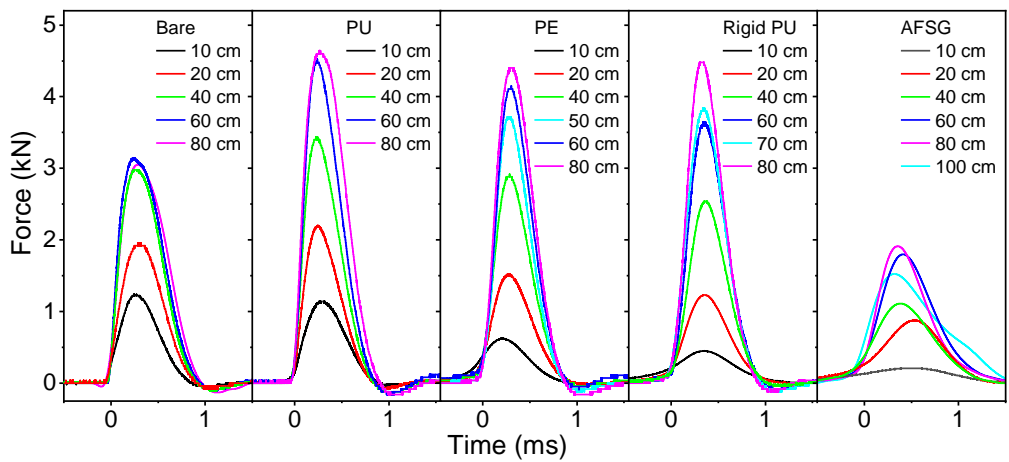
Figure S25. Force-time curves of impacted glasses protected with nothing, PU foam, PE foam, rigid PU foam, and AFSG respectively.
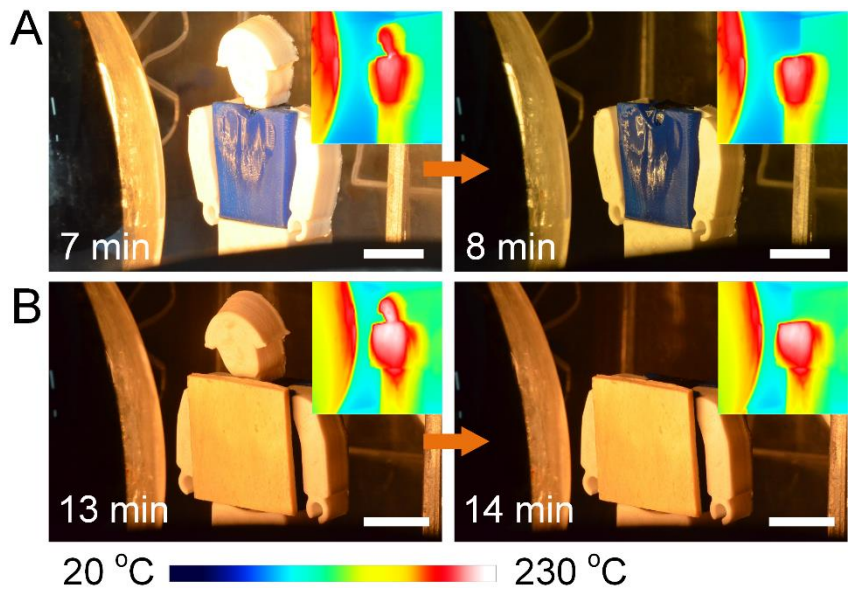
Figure S26. Optical images showing the heads dropping of toy men. Scale bars, 20 mm. Insets showed corresponding infrared images.
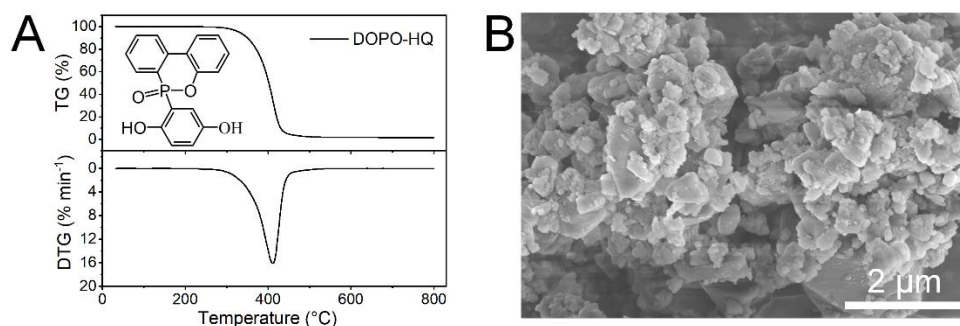
Figure S27. Characterization of DOPO-HQ nanoparticles. (A) TG and derivative thermogravimetric (DTG) curves of DOPO-HQ nanoparticles (Inset showed the chemical structural formula of DOPO-HQ). (B) SEM image of DOPO-HQ nanoparticles.
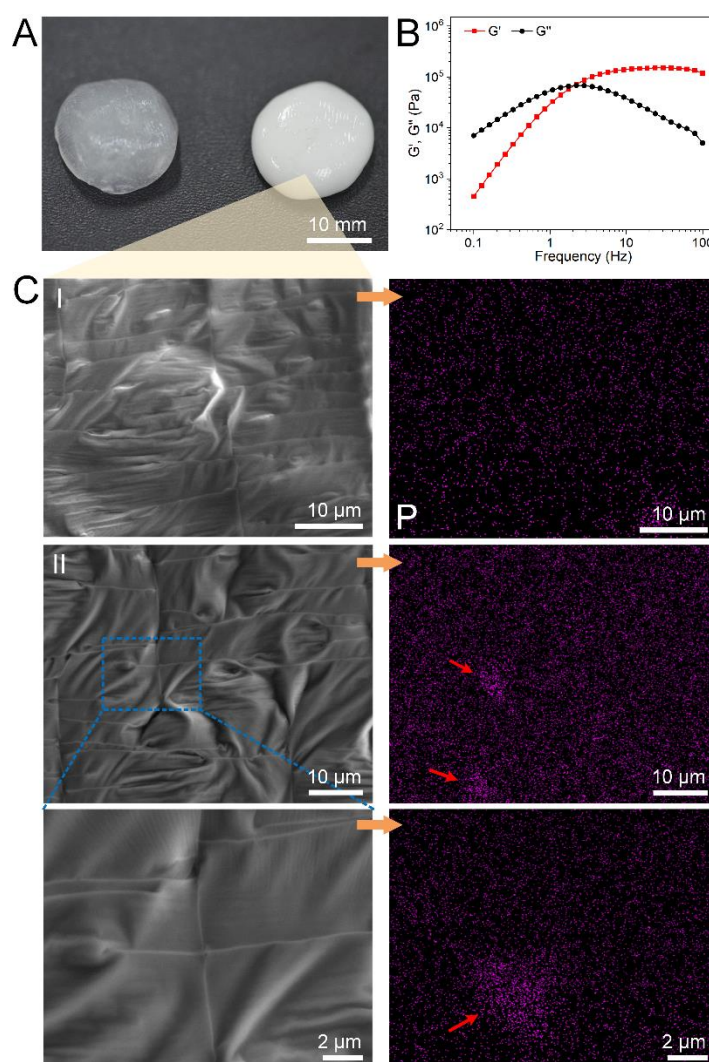
Figure S28. Characterization of SSG mixed with 7 phr DOPO-HQ. (A) Photographs of SSG (left side) and SSG mixed with 7 phr DOPO-HQ (right side). (B) Rheological property of SSG mixed with 7 phr DOPO-HQ. The dependence of storage modulus (G′) and loss modulus (G″) on oscillating shear frequency under strain of 0.1%. (C) SEM images of two sites of SSG mixed with 7 phr DOPO-HQ and corresponding EDS maps showing the distribution of phosphorus.

DOPO-HQ nanoparticles were dispersed in ethanol along with SSG and then infiltrated into ANF scaffolds to prepare F-AFSG. After the elimination of ethanol, SSG mixed with DOPO-HQ was obtained. As shown in Figure S28A, after the addition of 7 phr DOPO-HQ, SSG turned from translucent to white. Rheological test (Figure S28B) indicated that it still exhibited significant shear stiffing effect (G′ improved from 453 Pa to 117 kPa with frequency). Due to the cold-flow feature of SSG, DOPO-HQ nanoparticles were buried inside the matrix and could not be directly observed in SEM images (Figure S28C left side). But the distribution of phosphorus (P) element could be characterized by EDS maps. As shown in Figure S28C right side, the wide existence of P element in the two sites reflected homogenous distribution of DOPO-HQ in SSG. However, a small amount of nanoparticle aggregations indicated by red arrows were observed, which may result in stress concentration of F-AFSG.
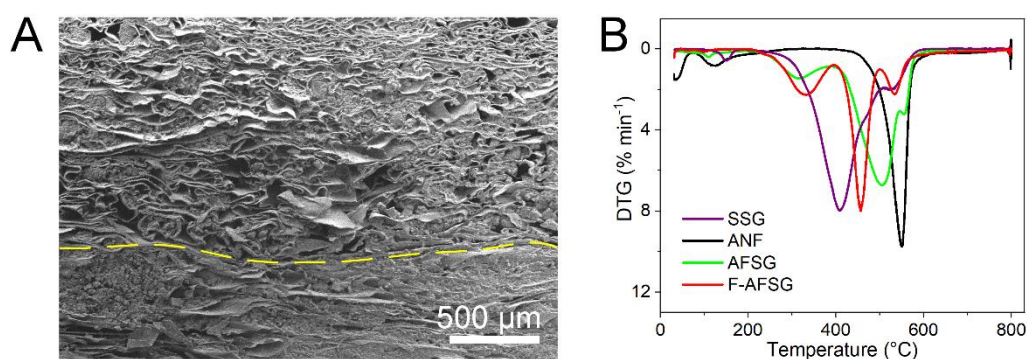
Figure S29. Characterization of F-AFSG. (A) SEM cross-section image of F-AFSG. The yellow dotted line denoted as the boundary of orthogonally laminated interface. (B) DTG curves of SSG, ANF, AFSG, and F-AFSG.
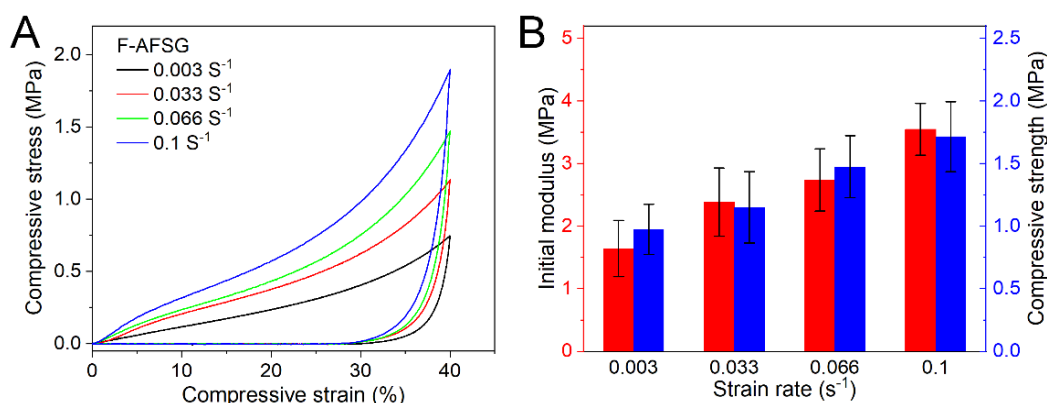
Figure S30. Rate-dependent compressive behavior of F-AFSG. (A) Compressive stress-strain curves of F-AFSG. (B) The dependence of initial modulus and compressive strength on strain rate of F-AFSG.

The compression property of F-AFSG was tested. Compared to AFSG (Figure 3B-C), both the initial modulus and compression strength of F-AFSG at specific strain rate improved obviously (Figure S30B). The enhanced mechanical property was ascribe to the introduction of DOPO-HQ nanoparticles, which could carry partial loads when F-AFSG was compressed. Furthermore, a small amount of nanoparticle aggregations (Figure S28C) was also responsible for the

improved strength. Nonetheless, the modulus and strength increased significantly from 1.64 MPa and 0.97 MPa at 0.003 s^{-1} to 3.55 MPa and 1.71 MPa at 0.1 s^{-1} (Figure S30B), which indicated a slight effect of DOPO-HQ on the rate-dependent compressive behavior.
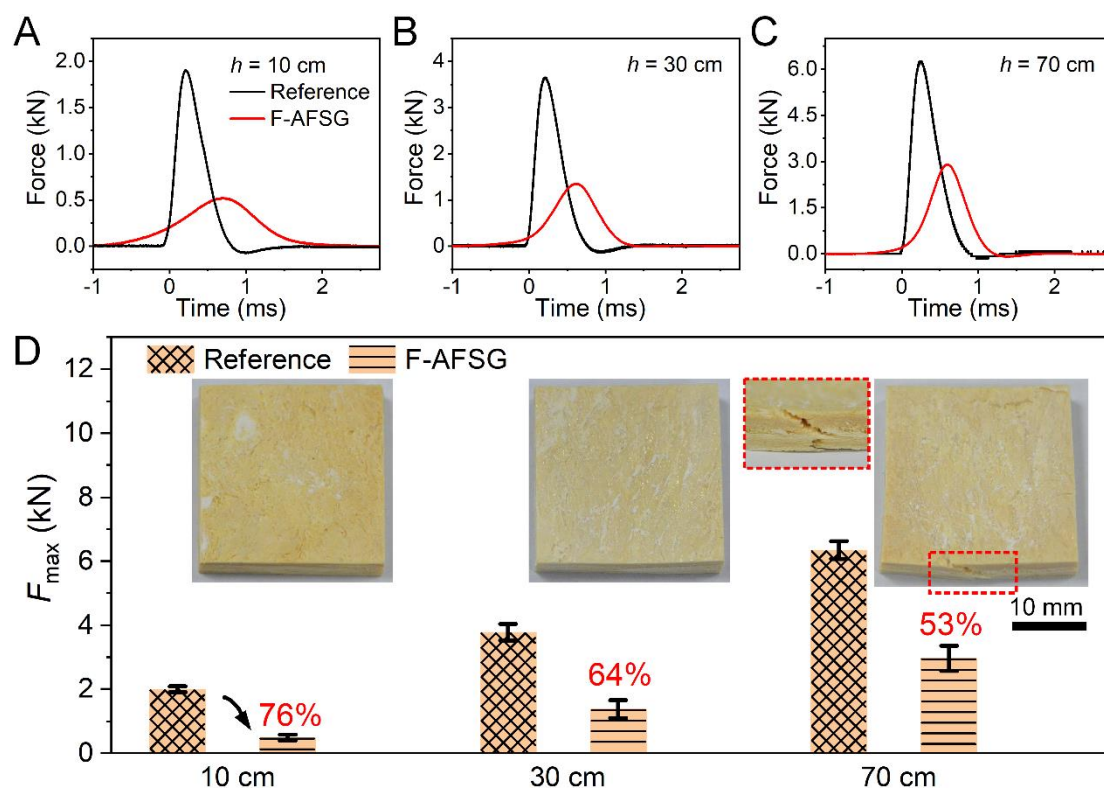
Figure S31. Anti-impact performance of F-AFSG. (A-C) Force-time curves of F-AFSG during impact process from heights of (A) 10 cm, (B) 30 cm, and (C) 70 cm, respectively. (D) Corresponding F_{max} of F-AFSG estimated from (A-C). (The insets represented surface morphologies of F-AFSG after impact. Red texts represented percentage of force attenuation)

As shown in Figure S31A-C, F-AFSG effectively reduced the force peaks and prolonged the impact times of reference conditions at 10-70 cm. Corresponding percentages of force attenuation were estimated in Figure S31D. The values reached 76% and 64% at 10 and 30 cm respectively, which were slightly lower than that of AFSG (Figure 4H). The whole structures of F-AFSGs also kept intact at this impact heights (insets of Figure S31D). When the height increased to 70 cm, interlayer crack appeared. The force attenuation effect had an obvious degeneration (53%) compared to AFSG (65%, Figure 4H). It was probably caused by the reduced loss modulus of SSG after the introduction of DOPO-HQ (Figure S28B and Figure 2F), which weakened energy dissipation of F-AFSG against high impact height. Overall, the impact force dissipation was still prominent (53%-76%) against 10-70 cm.
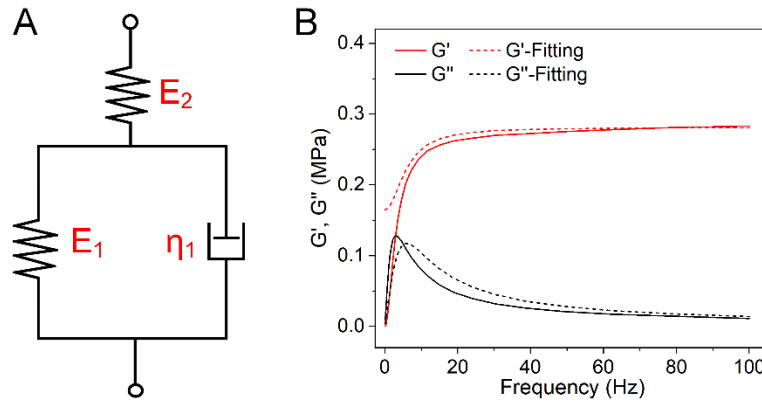
Figure S32. Constitutive model of SSG. (A) The standard linear solid model. (B) Experimental and fitting curves of storage modulus and loss modulus.
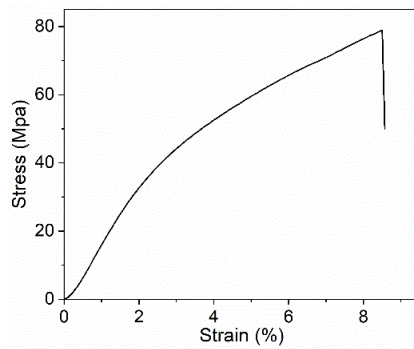
Figure S33. Tensile stress-strain curve of a single ANF sheet.
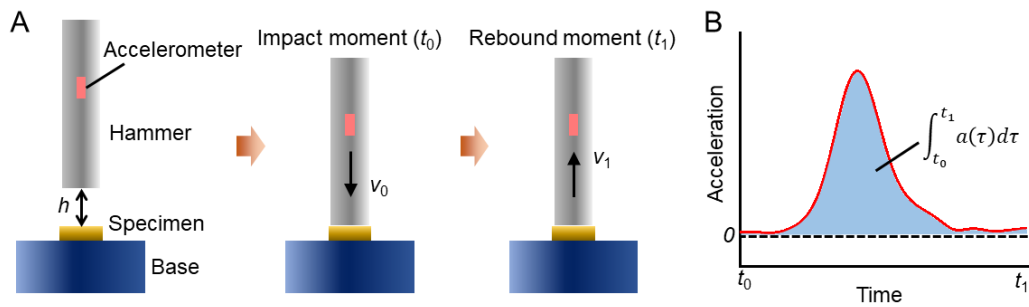
Figure S34. Schematic illustrating (A) the free-falling process of drop hammer and (B) corresponding integral of acceleration signal.
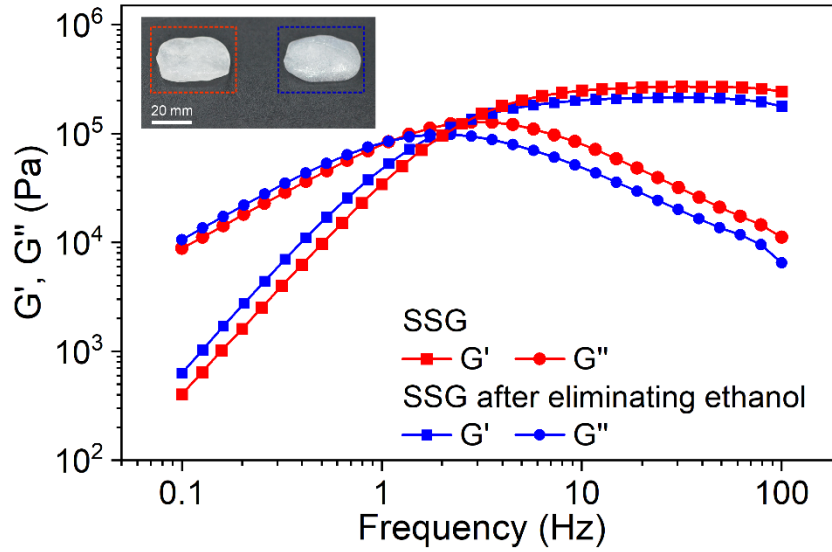
Figure S35. Rheological property of SSG after eliminating ethanol. The dependence of storage modulus (G′) and loss modulus (G″) on oscillating shear frequency under strain of 0.1%. Samples in red frame and blue frame represented the original SSG and SSG after eliminating ethanol, respectively.

Table. S1. The parameters of dimensions and masses of three highly filled AFSGs.

Number	Dimension (mm × mm × mm)	Mass (g)	Density (g cm^{-3})
1	30.76×30.91×5.10	2.9798	0.6145
2	30.44×30.39×5.05	2.7283	0.5840
3	30.95×30.53×4.93	2.7934	0.5997

Table. S2. The parameters of thermal conductivities of selected materials.

Material	Thermal conductivity (W m^{-1} k^{-1})
Epoxy	0.21
PDMS	0.12
Eco-flex	0.20
Poplar wood	0.18
Silicone rubber	0.29
Gelatin	0.54
Natural rubber	0.58
Leather	2.00
AFSG	0.093

Supplemental Notes

Note S1. Finite-element models of SSG and ANF scaffolds

For SSG, a standard linear solid (SLS) model[9] (Figure S32A) was used to simulate its rate-dependent mechanical behavior, which consisted of two springs (E_1, E_2) and a damper (η_1). The constitute equation was described as follow,

$$\sigma + p_1\dot{\sigma} = q_0\varepsilon + q_1\dot{\varepsilon} \qquad \text{(Equation 1)}$$

Where σ and ε denoted as stress and strain respectively. Superscript represented derivation

to time. p_1, q_0, q_1 were as follow,

$$p_1 = \frac{\eta_1}{E_1+E_2} \ , \ q_0 = \frac{E_1 E_2}{E_1+E_2} \ , \ q_1 = \frac{E_2 \eta_1}{E_1+E_2}$$ (Equation 2)

The values of p_1, q_0, q_1 were acquired by fitting the rheological curves in Figure S32B according to the following relationship,

$$G' = \frac{q_0 + p_1 q_1 \omega^2}{2(1+\mu)(1+p_1^2 \omega^2)} \ , \ G'' = \frac{(q_1 - p_1 q_0)\omega}{2(1+\mu)(1+p_1^2 \omega^2)}$$ (Equation 3)

Where G', G'', μ, and ω belonged to storage modulus, loss modulus, Poisson's ratio, and angular frequency, respectively.

ANF scaffold was approximately treated as an elastic model. The tensile property of a single ANF sheet was shown in Figure S33, where elastic modulus and elongation at break were 16.6 GPa and 8.5% respectively.

Note S2. Energy absorption during impact process

The energy absorption abilities of all materials were evaluated by calculating the kinetic energy difference of hammer in drop impact test. Specifically, the hammer was assumed to free-fall from specific height (h =70 cm) to specimen without any frictional resistance (Figure S34A). According to energy conversation law, the initial kinetic energy (E_0) and initial velocity (v_0) of hammer at impact moment (t_0) were represented as follow respectively,

$$E_0 = mgh \ , \ v_0 = \sqrt{2gh}$$ (Equation 4)

Where m and g belonged to the mass of hammer (0.55 kg) and gravity acceleration (9.8 m s^{-2}) respectively. The velocity (v_1) of hammer at rebound moment (t_1) was as follow,

$$v_1 = v_0 - \int a \, dt = \sqrt{2gh} - \int_{t_0}^{t_1} a(\tau) \, d\tau$$ (Equation 5)

Where the second term denoted as the integral of acceleration (a) over entire impact-rebound time (Figure S34B and Figure S22). Thus the energy absorption (ΔE) of specimen to hammer during impact process could be described as follow,

$$\Delta E = E_0 - \frac{1}{2}mv_1^2 = mgh - \frac{1}{2}m\left(\sqrt{2gh} - \int a \, dt\right)^2$$ (Equation 6)

Note S3. Orthogonally laminating structure and densification under ~80% compression

As shown in Figure 1E and Figure 4H inset, the orthogonally laminating structure could dissipate partial energy through interlayer sliding when subjecting to impact. Furthermore, it could effectively impede cracks propagation along oriented ANF scaffolds and alleviate the fracture degree of AFSG, which provided better impact protection than monolayer structure. To illustrate this point more intuitively, AFSGs under ~60% compression with monolayer and laminating structure were prepared respectively to evaluate the anti-impact ability. As shown in Figure S15, after being impacted from 50 cm height, the monolayer structure suffered severe fracture failure along the oriented ANF scaffold (red circles in Figure S15D inset), whereas only a shallow crack appeared in the orthogonally laminating structure (Figure S15B inset). Although the force peak of monolayer AFSG was low (cyan curve in Figure S15D), the extensive crack propagation caused a poor protective utility against high impact energy. In addition, the thermal conductivities of monolayer structure and laminating structure were measured to be 0.122 and 0.125 W m^{-1} k^{-1} respectively (Figure S16), which reflected a negligible effect of structural layout

on thermal performance. Therefore, the orthogonally laminating structure was used to prepare AFSG.

In addition, AFSGs under low compression of ~60% and ~40% were prepared to compare the thermal and impact performances with ~80% compression. As shown in Figure S14C and F, the voids possessed larger pore size due to low densification level compared to ~80% compression (Figure S3F), which was not conductive to weakening internal air convection. The large pore size also tended to reduce the amount of voids in AFSG in terms of specific thickness. Furthermore, massive SSG micro-blocks with large volume were easily infiltrated into the ANF scaffolds, leading to an increase in density (~40% for 0.55 g cm^{-3}; ~60% for 0.57 g cm^{-3}; ~80% for 0.46 g cm^{-3}. Figure S14 and Figure 5E). The large SSG micro-blocks also improved thermal transfer rate. Therefore, both the AFSGs under ~60% and ~40% compressions had higher thermal conductivities (0.125 and 0.098 W m^{-1} k^{-1}, Figure S16) than AFSG under ~80% compression (0.093 W m^{-1} k^{-1}). In addition, when subjected to mechanical impact, the loose ANF scaffolds were incapable of restricting the expansion of large SSG micro-blocks (Figure S14C and F), which resulted in serious central depression and cracks propagation in these two AFSGs (insets of Figure S15B-C). Therefore, ~80% compression was used to prepare AFSG.

Supplemental References
1. Li, X., Dong, G.Q., Liu, Z.W., and Zhang, X.T. (2021). Polyimide aerogel fibers with superior flame resistance, strength, hydrophobicity, and flexibility made via a universal sol-gel confined transition strategy. ACS Nano *15*, 4759-4768. 10.1021/acsnano.0c09391
2. Du, A., Wang, H.Q., Zhou, B., Zhang, C., Wu, X.L., Ge, Y.T., Niu, T.T., Ji, X.J., Zhang, T., Zhang, Z.H., et al. (2018). Multifunctional silica nanotube aerogels inspired by polar bear hair for light management and thermal insulation. Chem. Mater. *30*, 6849-6857. 10.1021/acs.chemmater.8b02926
3. Cao, X., Liu, J., Cao, X., Li, Q., Hu, E., and Fan, F. (2015). Study of the thermal insulation properties of the glass fiber board used for interior building envelope. Energy Build. *107*, 49-58. 10.1016/j.enbuild.2015.08.007
4. Yang, Y., Cheng, X.Y., Chen, Z.F., Fu, R.L., Chen, Z., Qiu, J.L., and Su, D. (2013). Influence of density on the thermal conductivity of fiberglass felt. Adv. Mater. Res. *628*, 33-6. 10.4028/www.scientific.net/AMR.628.33
5. Zhan, H.J., Wu, K.J., Hu, Y.L., Liu, J.W., Li, H., Guo, X., Xu, J., Yang, Y., Yu, Z.L., Gao, H.L., et al. (2019). Biomimetic carbon tube aerogel enables super-elasticity and thermal insulation clear wood toward high-performance building materials. Chem *5*, 1871-1882. 10.1016/j.chempr.2019.04.025
6. Jia, C., Chen, C.J., Mi, R.Y., Li, T., Dai, J.Q., Yang, Z., Pei, Y., He, S.M., Bian, H.Y., Jang, S.H., et al. (2019). Clear wood toward high-performance building materials. ACS Nano *13*, 9993-10001. 10.1021/acsnano.9b00089
7. Wu, J.W., Sung, W.F., and Chu, H.S. (1999). Thermal conductivity of polyurethane foams. Int. J. Heat Mass Tran. *42*, 2211-2217. 10.1016/S0017-9310(98)00315-9
8. Li, T., Song, J.W., Zhao, X.P., Yang, Z., Pastel, G., Xu, S.M., Jia, C., Dai, J.Q., Chen, C.J., Gong, A., et al. (2018). Anisotropic, lightweight, strong, and super thermally insulating nanowood with naturally aligned nanocellulose. Sci. Adv. *4*, eaar3724. 10.1126/sciadv.aar3724

9. Zhao, C.Y., Wang, Y., Ni, M.Y., He, X.K., Xuan, S.H., and Gong, X.L. (2021). Dynamic behavior of impact hardening elastomer: a flexible projectile material with unique rate-dependent performance. Compos. Part. A-Appl. S. *143*, 106285. 10.1016/j.compositesa.2021.106285